Robles, G., Fresno, J. M., & Giannetti, R. (2017). Ultrasonic bone localization algorithm based on time-series cumulative kurtosis. ISA Transactions, 66, 469–475.

DOI: 10.1016/j.isatra.2016.09.012

Ultrasonic bone localization algorithm based on time-series cumulative kurtosis

Guillermo Robles[a,*], José Manuel Fresno[a], Romano Giannetti[b]

[a] *Dept. Electrical Engineering, Universidad Carlos III de Madrid, 28911 Leganés, Madrid, Spain.*
[b] *Dept. of Electronics and Automatization, Universidad Pontificia Comillas de Madrid, 28015 Madrid, Spain.*

Abstract

The design and optimization of protective equipment and devices such as exoskeletons and prosthetics have the potential to be enhanced by the ability of accurately measure the positions of the bones during movement. Existing technologies allow a quite precise measurement of motion — mainly by using coordinate video-cameras and skin-mounted markers — but fail in directly measuring the bone position. Alternative approaches, as fluoroscopy, are too invasive and not usable during extended lapses of time, either for cost or radiation exposure. An approach to solve the problem is to combine the skin-glued markers with ultrasound technology in order to obtain the bone position by measuring at the same time the marker coordinates in 3D space and the depth of the echo from the bone. Given the complex structure of the bones and the tissues, the echoes from the ultrasound transducer show a quite complex structure as well. To reach a good accuracy in determining the depth of the bones, it is of paramount importance the ability to measure the time-of-flight (TOF) of the pulse with a high level of confidence. In this paper, the performance of several methods for determining the TOF of the ultrasound pulse has been evaluated when they are applied to the problem of measuring the bone depth. Experiments have been made using both simple setups used for calibration purposes and in real human tissues to test the performance of the algorithms. The results show that the method used to process the data to evaluate the time-of-flight of the echo signal can significantly affect the value of the depth measurement, especially in the cases when the verticality of the sensor with respect to the surface causing the main echo cannot be guaranteed. Finally, after testing several methods and processing algorithms for both accuracy and repeatability, the proposed cumulative kurtosis algorithm was found to be the most appropriate in the case of measuring bone depths in-vivo with ultrasound sensors at frequencies around 5 MHz.

Keywords: ultrasound, time of flight, biomedical transducers, ultrasonic transducers, localization

1. Introduction

Accurate measurement of the dynamics of the musculoskeletal system is limited by the problem of measuring the position of the bones during dynamic and weight-bearing activities. Existing methods to measure motion in these conditions include optically-tracked markers [1] and worn goniometric devices [2]. Both methods measure basically the skin position, and although sometimes it is possible to use them to mark patches of skin with very superficial bones, they are not generally able to give the necessary bone position accuracy [3]. For example, it would be very useful to be able to measure real-time position of the pelvis bones of subjects forced to stay in wheelchairs, in order to optimize the stance to avoid or minimize injuries; or, it could be devised an actuator able to automatically manage the tightness of a knee bracket responding to the bones movements in real-time. In those cases, the measurement of the position of markers on the skin can have relatively limited relationship with the underneath bone position.

One of the possible approaches to a wearable, non-invasive bone depth measurement is using ultrasound (US) sensors in a similar way as they are used to detect failures in pipes and mechanical structures [4]. To perform the measurement, an US sensor is rigidly associated to each one of the infrared markers used by the 3D tracking system, and a set of such compound sensors will be positioned around the limb for estimating the position of the bone, see Figure 1.

Notice how, due to the movement of the muscle and fat tissue around the target bone, the angular orientation of the US sensor will be difficult to predict and estimate. The measurement strategy will be oriented to measure the smallest distance between the skin surface (where the US sensor is attached with an adhesive or an external restraint system) and the bone underneath.

The big difference in the acoustic impedance between soft tissues and bone tissues in human bodies will give a very strong echo to incident acoustic waves, smaller only than the echoes generated by a tissue/air interface, where the acoustic impedance difference is even higher. For ex-

*Corresponding author
Email addresses: grobles@ing.uc3m.es (Guillermo Robles), jfresno@ing.uc3m.es (José Manuel Fresno), romano@comillas.edu (Romano Giannetti)

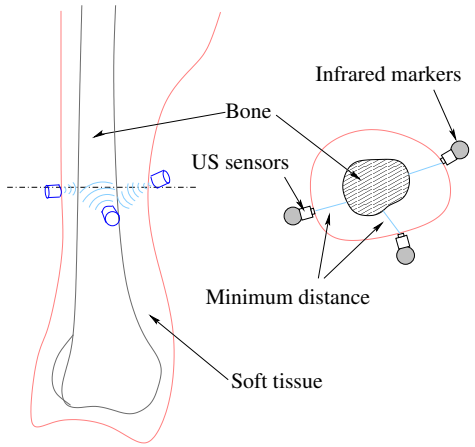

Figure 1: Triangulating a bone position by three coupled optical (IR) and ultrasound (US) sensors.

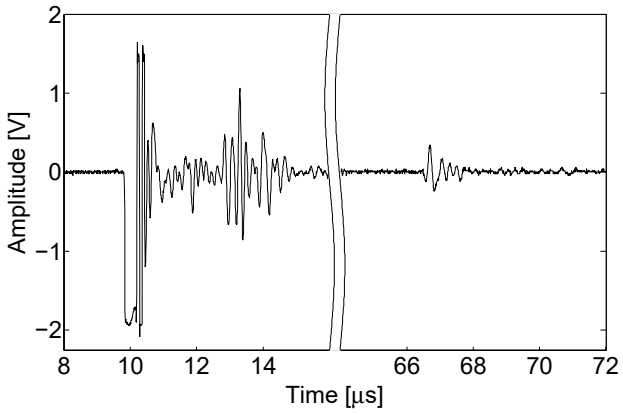

Figure 2: An example of echo from a bone measured in a human subject; the sensor was on the skin of the external part of the thigh. The ultrasonic pulse at 10 µs is the emitter pulse, and the pulse between 66 and 68 µs is the echo from the femur.

ample, at a frequency of 1 MHz, the acoustic impedance of bones is around 7.8×10^6 Rayls, while the different soft tissues (fat, blood, muscle) range from 1.35 to 1.75 MRayls [5]— so the echoes from the bone/soft tissue are bond to be quite stronger than the echoes caused by different tissues interfaces. The only difficult echoes could come by extremely porous cancellous bones [6], where the reflected pulses would be much weaker, but this case is not common in practical applications, so it does not seriously reduce the effectiveness of the method.

Even though the echoes are strong, the fact that there are multiple reflections involved, and lateral conduction in the bones [7], the received signal is not so sharp, and the detection of the significant point for the echo onset is not trivial; in Figure 2, the raw data from the echo of a human femur is shown. The effect of multipath reflections is minimized in the picking of the onset of the echo determining which is the first front wave arriving to the sensor. This is best done with methods based on the energy of the signal as shown in Section 3. The reflected waves from the periosteal surface of the bone are indeed very complex due to the non-planar and rough structure of the surface itself [8]; a detailed study of such reflections is needed when the objective is to image the bone geometry [9] and/or detecting additional information as density or elasticity [10]. In our application, we are interested in determining the depth (minimum path) of the bone surface, with independence of the angle of incidence of the probe — which indeed shows a quite broad angle of emission which, in turn, simplifies the problem of the analysis of the echo.

Most studies involving ultrasound techniques are devoted to the measurement of the propagation of sound through bone. Mass and architecture of bones can be determined by the velocity or speed of sound and the attenuation of the ultrasound wave in frequency or broadband ultrasound attenuation (BUA) [11], [12]. The measurement of time-of-flight is almost restricted to the axial and circumferential propagation of the waves in bones to determine their geometry, elasticity and mineralization, [13]. The calculation of the TOF is done through simple techniques such as the time between the pulse and echo peaks or between the pulse and the first inflection point of the first echo without paying much attention to the signal to noise ratio. This paper proposes the use of different algorithms already tested in other fields such as geology, [14, 15, 16], or engineering to face the problems found in noisy environments and with multi-propagation paths, [17, 18, 19].

2. Instrumentation and measurements

In choosing the ultrasound signal frequency, a compromise must be done between the availability and price of the transceiver (which are cheaper and easier to find for low frequencies), and the resolution that the resulting wavelength in the soft tissue will enable. Working in the 2–10 MHz range, with a wavelength in soft tissues of about 0.75–0.15 mm, has been chosen as a good compromise.

The selected transducer is an Olympus V609-RB ultrasound bidirectional device, which costs around 300 USD; its nominal operating frequency (5 MHz) is well into the selected range. In the experiments, it was driven with an Olympus manually controlled ultrasonic pulser-receiver (5072PR) and the ultrasonic signal was visualized and recorded using a Tektronix TDS 5104 Digital Storage Oscilloscope (DSO). The DSO was set with a resolution of 8 ns and a time span of 100 µs. Figure 3 depicts the structure of the measurement setup.

3. Time-of-flight algorithms

This section explains the fundamental principles and groundwork of the algorithms working on examples of measurements taken in a human thigh. The signals have an initial pulse generated by the excitation that is used to

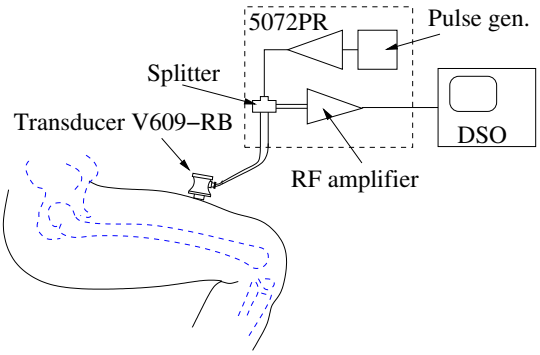

Figure 3: Setup of the measurement system shown when taking the measurement of bone depth of a femur bone in a human thigh.

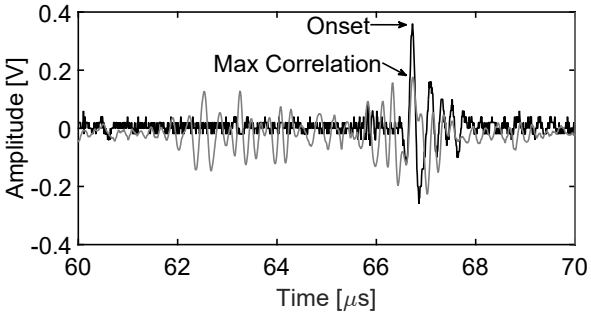

Figure 4: Detail of the onset determined by the cross correlation algorithm to determine the time-of-flight. The black plot corresponds to the echo and the grey plot to the cross correlation.

calculate the starting time with every algorithm. This pulse provokes some immediate reflections on the interfaces between the surface sensor and the epidermis tissue and between the different layers of the epidermis and dermis tissues, see left pulse in Figure 2. To reject these reflections, the trigger of the oscilloscope is set to 10 μs so the excitation pulse starts at this time and extinguishes before 16 μs; from here on, the algorithm searches for the onset of the echo in the bone. Alternatively, the selected signal has a small echo before the actual one due to inhomogeneous sections of the muscle and fat tissues close to the bone. This example with the perturbation has been chosen to test the performance of the algorithms and show that they may be deceived resulting in early pickings of the onset of the pulse.

3.1. Cross correlation

The classical method to calculate the time delay between two signals, s_1 and s_2, is based on the application of cross correlation techniques and finding the shift of the maximum of $R_{12}(n)$ defined as:

$$R_{12}(n) = \sum_{m=-N/2}^{N/2-1} s_1(m+n)s_2(m) \qquad (1)$$

where N is the total number of samples.

This method has been extensively applied in many fields with good results, [20, 21, 22, 23]. However, the reflections due to multipath propagation and interferences due to reflections on concave surfaces can yield larger peaks than the direct front wave in ultrasonic signals. This means that the maximum of the correlation function would choose these peaks and would give a delayed picking of the signal. Using the preprocessing techniques presented in the generalized correlation method [24], such as the Roth processor, the smoothed coherence transform (SCOT) and the phase transform (PHAT) would not help in obtaining good results since they are aimed at reducing the effect of white noise.

Figure 4 shows where the cross correlation algorithm would detect the onset of the echo of a signal taken on a human thigh. In this case, s_1 is the pulse emitted by the US sensor and s_2 is the received echo. The output of the cross correlation gives directly the time delay between s_1 and s_2. Then, as s_1 starts at 10 μs, R_{12} has been manually shifted 10 μs to plot the cross correlation (grey line) and the echo (black line) in the same figure.

3.2. Maximum peak

In this algorithm, the time-of-flight is measured from the peak of the excitation pulse to the peak of the reflected wave so the results would be very similar to those given by the correlation methods. This is the most straightforward method and relies in the fact that a fast rising pulse creates an echo with a peak in the front wave. As with the correlation, this is true under ideal conditions in which multipath echoes are strongly damped, the media is homogeneous and the surface where the echo is reflected is normal to the incident wave. Under these circumstances the results would be repeatable and precise, in the sense that their standard deviation will be small, but not necessarily accurate, or close to the correct solution. The accuracy will depend on the rise time of the front wave of the echo and, consequently, on its attenuation, and change of slope, through the length of the media. Any deviation from these conditions would induce systematic and random errors to the measurements jeopardizing the robustness of this method. Figure 5 shows an example of the time-of-flight calculation in a measurement taken on human thigh.

3.3. Minimum energy

The calculation of the cumulative energy, shown in Equation (2), is a well-known technique to detect sharp changes in the signal, [15]. $E_c(n)$ is the cumulative energy up to sample n, and s is the signal. The algorithm starts with a certain and constant positive slope due to the accumulation of the energy of noise. This slope changes abruptly when the energy of the first impulse of the echo is added to the accumulation. The key is to find where

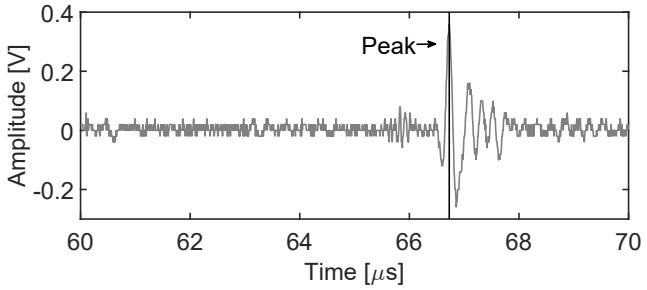

Figure 5: Detail of the time of occurrence of the maximum peak to determine the time-of-flight in a signal taken on a human thigh. The vertical line represents the onset of the signal using the maximum peak algorithm.

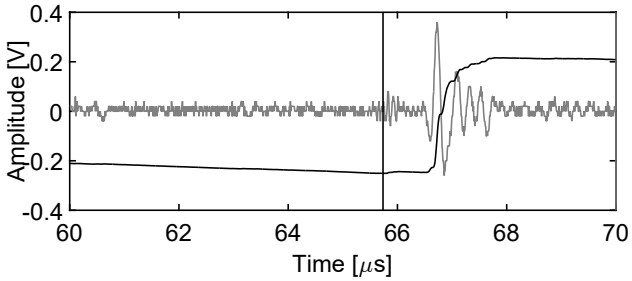

Figure 6: Detail of the time of occurrence of the minimum energy in the same signal as before. The vertical line represents the erroneous onset of the signal using the minimum energy algorithm. The cumulative energy in Equation (3) is also plotted to show its evolution.

exactly starts that change of slope because small perturbations before the onset of the signal can deceive the algorithm.

To mitigate this drawback, a line with negative slope is added to this energy so the point in which the signal starts turns to be the minimum of the function in Equation (3):

$$E_c(n) = \sum_{m=1}^{n} s^2(m) \tag{2}$$

$$E_{neg}(n) = E_c(n) - a \cdot n\frac{E_N}{N} = \sum_{m=1}^{n}\left(s^2(m) - a \cdot n\frac{E_N}{N}\right) \tag{3}$$

where E_N is the total energy of the signal, N is the total number of samples and a is a constant that pulls the absolute minimum further down in case there are several minima close to the correct one. Figure 6 shows the time of the echo in the two experiments considering the parameter $a = 1$. This plot shows a small pulse before the actual echo resulting in an early picking of the signal so the parameter a should be increased to pull the slope to more negative values and giving more weight to minima closer to the actual onset of the echo. This small pulse is present in some of the signals taken on a human thigh (Section 4.3) and is due to inhomogeneous sections of the muscle, fat tissues close to the bone and depends on the angle of incidence.

3.4. Akaike information criterion (AIC)

This method has been extensively used in the localization of earthquakes by detecting the arrival of the P-wave in seismic signals, [14], ultrasound detection, [15], and electrical engineering, [17, 18]. It considers that both the portion of the signal corresponding to noise and the segment with seismic signal, or in this case, the echo, are autoregressive (AR) processes. In general, noise can be represented with a low order AR process whereas the echo will need a noticeable larger number of coefficients to have an accurate model. The AIC determines the best order to fit AR processes, hence, analyzing the evolution of the number of coefficients would give the exact time when the onset of the echo occurs. Another possibility, avoiding the calculation of the AR order, is the direct application of the AIC to two segments of the ultrasonic signal, from sample 1 to n and from $n+1$ to N, [18]. The AIC is defined as,

$$AIC(n) = n\cdot\ln[\sigma^2(1,n)]+(N-n-1)\cdot\ln[\sigma^2(n+1,N)] \tag{4}$$

where

$$\sigma^2(1,n) = \frac{1}{n}\sum_{m=1}^{n}[s(m) - \bar{s}(1,n)]^2 \tag{5}$$

and

$$\sigma^2(n+1,N) = \frac{1}{N-n-1}\sum_{m=n+1}^{N}[s(m)-\bar{s}(n+1,N)]^2 \tag{6}$$

are the variances of the samples in the segments and $\bar{s}(\cdot)$ is the mean value of the signal in the considered interval.

Figure 7 shows the performance of the Akaike information criterion for the same signal. This method finds the onset of the echo as a global minimum of Equation (4) so the analyzed window should encompass closely the onset of the signal, otherwise, the global minimum would be very likely far from the correct solution. Again, the plot in Figure 7 shows that this method would give early pickings in signals with noticeable perturbations before the onset of the pulse.

3.5. Minimum time series cumulative kurtosis

This method is a modification of the picking algorithm presented in [16] in which the estimated cumulative kurtosis is analyzed in a sliding time window. Considering that the pre-triggered signal is a stationary process, the mean and variance are time invariant and higher-order statistics would be constant. Any new value belonging to a non-Gaussian distribution such as the inception of the pulse signal would induce an increment in the kurtosis, Equation (7). When more samples of the pulse arrive to the detector, the 4th-moment increases as these new values

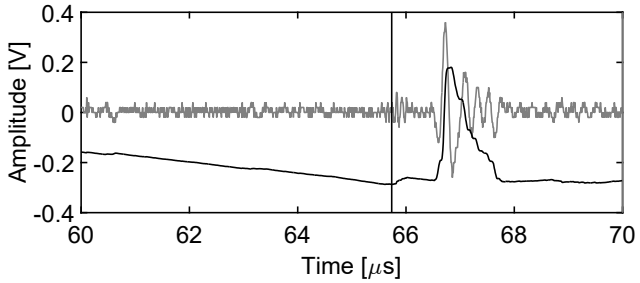

Figure 7: Time of occurrence using the AIC algorithm represented with a vertical line. Again, in this example, the algorithm detects a false echo close to the actual one.

Table 1: Statistical parameters for two 1000-samples set containing noise and the onset of the echo.

	Mean (mV)	Std. dev. (mV)	Kurtosis
Noise	4	14.6	2.78
Onset	4.3	23.6	64.03

are placed at the tails of the Gaussian distribution previously defined by the noise.

$$k(n) = \frac{\frac{1}{n}\sum_{m=1}^{n}[s(m) - \bar{s}]^4}{\left(\frac{1}{n}\sum_{m=1}^{n}[s(m) - \bar{s}]^2\right)^2} \tag{7}$$

Figure 8 is a clear example on what happens with the estimation of the kurtosis. The histogram represent the number of samples that fall in certain amplitudes from a total of 1000 samples. The bars in black correspond to the distribution of a portion of the total signal where there is only noise (selection "noise") in Figure 9. The bars in light grey conform the distribution of a part of the signal that selects the onset of the echo (selection "noise and echo onset"), Figure 9. The amplitudes of some points in this sub-signal are ten times larger than the amplitude of noise so the tails of the distribution in the histogram are extended changing its shape and hence the kurtosis. Table 1 shows the mean, standard deviation and kurtosis of the two 1000-samples sets. Both cases have almost the same mean value, while the standard deviation and the kurtosis are larger in the case of the echo, as expected. The kurtosis for the noise is close to 3 so the shape of that distribution is very close to Gaussian, while in the case of the onset of the echo the kurtosis value is much larger, 64.03. Notice that the change in the kurtosis is more dramatic than the change in the standard deviation. As the energy of the signal is related to the standard deviation, it can be inferred that monitoring the changes in the kurtosis would be more effective in finding the TOF than any energy-based method.

Several samples of the non-Gaussian signal are needed for the cumulative kurtosis to reach the maximum and af-

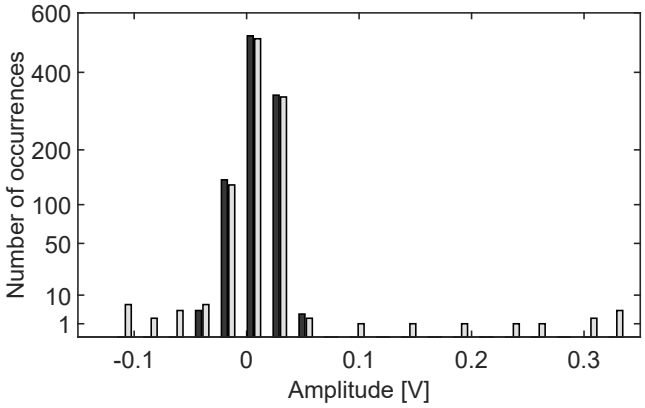

Figure 8: Histogram of two sets of 1000 samples from one of the measurements taken on a human thigh. The bars in black are noise data while the bars in light grey correspond to noise and the onset of the echo signal. The vertical axis has been modified to show low numbers of occurrences.

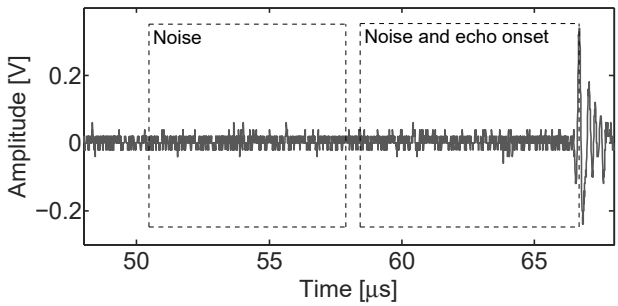

Figure 9: Plot of an echo where 1000 samples of noise and 1000 samples up to the onset of the echo are highlighted to show the performance of the kurtosis algorithm.

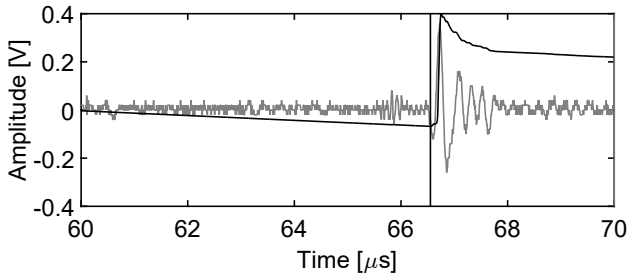

Figure 10: Time of occurrence using the Kurtosis algorithm represented with a vertical line.

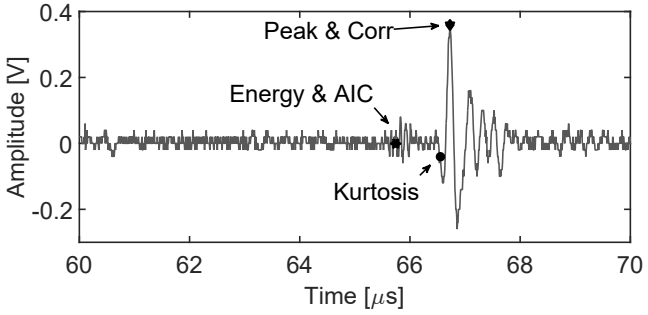

Figure 11: Onset times for all algorithms summarized in the same figure. AIC and minimum energy algorithms, on the one hand, and peak and cross correlation, on the other hand, give the same time whereas the kurtosis gives the most accurate onset of the pulse.

ter that it decreases again to around 3 when the impulsive signal disappears, Figure 10. Notice that the maximum kurtosis does not coincide with the signal onset but at the point in time when the cumulative kurtosis starts to soar.

The picking can be determined by setting a threshold to the kurtosis or by calculating its maximum derivative. Unfortunately, the threshold would systematically give late pickings and the maximum derivative can be so noisy that, in most cases, would yield unreliable results. The approach followed in this paper is the same as the shown in Equation (3) which is to add a negative slope line to highlight the bend of the function as a local minimum. Equation (7) is, thus, modified to

$$k(n) = \frac{\frac{1}{n}\sum_{m=1}^{n}[s(m)-\bar{s}]^4}{\left(\frac{1}{n}\sum_{m=1}^{n}[s(m)-\bar{s}]^2\right)^2} - n\frac{K}{n_K} \qquad (8)$$

where, in this case, K is the maximum cumulative kurtosis and n_K is the sample where that maximum occurs. This modification gives a plot that decreases with a constant slope when the original signal is noise reaching a minimum in the onset of the pulse, from this instant the values of $k(n)$ in Equation (8) increase until the pulse finishes.

Finally, Figure 10 also shows that the cumulative time-series kurtosis is insensible to the small perturbation that appears before the actual echo, contrary to what happened with the minimum energy and AIC algorithms.

3.6. Summary

Figure 11 summarizes all the results for the studied case. Notice that the signal has a noticeable oscillation slightly before the onset of the main echo that is deceiving the AIC and minimum energy algorithms. The maximum and cross correlation, as pointed out before, give systematic late pickings so the best option would be the algorithm based on the cumulative kurtosis. This result has to be supported by more signals and different configurations which is done in the next section.

4. Results

The test benchmark consisted on measurements conducted in different media, boundary conditions and positions of the ultrasonic sensors which defined six test environments.

The algorithms were applied to sets of ten signals obtained in gel pads and a human thigh. The first two experiments are aimed at the evaluation of the algorithms in a controlled environment in which we have a homogeneous media of a known thickness. The experiment in human flesh represents a more realistic case in which different tissues can be found before reaching the bone and the thickness in unknown. Then, the first experiments help in the calibration of the method while the other experiment tests the algorithms with real measurements. In each configuration, the sensor is placed on the samples either vertically aligned, to have a direct reflection of the echo, or slanted, so the path of the echo is slightly different, see Figure 13. The purpose is to test the behavior of the measuring system and the algorithms in those cases where the sensor has drifted from its original position due to the movement of the subject. Ten consecutive measurements are taken in both positions and in all samples. Then, the average time-of-flight is calculated and compared with the actual one in the case of the gel pads. This average would give a measurement of the accuracy of the results, whereas the standard deviation of the times-of-flight would represent the repeatability of the algorithm.

4.1. Two gel pads with air interphase

Two pads 3 cm thick are placed one on the top of the other without any film gel in between, so that a thin air interphase will form and a reflection wave will be generated at the boundary between them. The pads are manufactured with a gel that has a transmission speed for ultrasonic waves in this frequency range of about 1500 m/s. This means that the echo reaches the interphase in 20 µs and the reflected pulse hits the sensor in 40 µs, see Figure 13 case *a*. An example of an echo with the sensor slanted is shown in Figure 12.

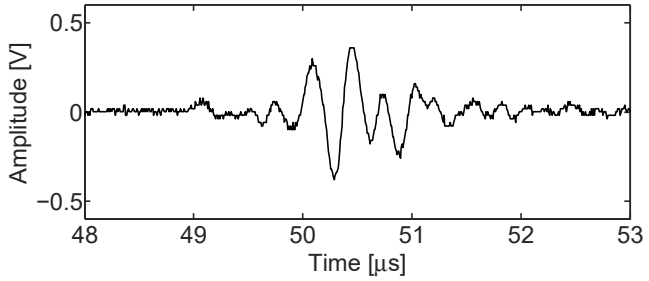

Figure 12: Echo in the air interphase when the sensor is slanted.

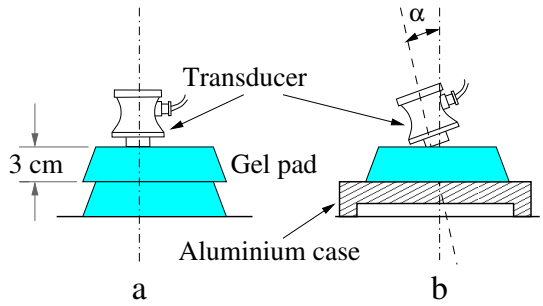

Figure 13: Experiment for the first set of data. The TOA measurement has been computed using several methods in the case of a couple of stacked gel pads (case *a*) with acoustic impedance similar to human soft tissues, and with a single gel pad positioned over a open metallic structure (*b*). In both cases the measurement were performed with the sensor vertically aligned and with the sensor slightly slanted.

Table 2 shows the results given by the algorithms for ten consecutive measurements in both positions: horizontal (or vertically aligned) and slanted. The most accurate algorithm would be the one with the closest average value to the actual thickness of the gel, 40 µs or 3 cm, and the best method, in terms of repeatability of the results, would be the one with the lowest standard deviation. With the sensor vertically aligned, the most accurate methods are: the proposed in this paper based on the cumulative kurtosis and the AIC with the same difference from the correct time, 40.02 µs and 39.98 µs, respectively. On the contrary, the best repeatability is given by the method based on the minimum cumulative energy followed by the cumulative kurtosis. When the sensor is slanted, the most accurate is again the kurtosis, with 40.14 µs, while the lowest standard deviation corresponds to the maximum peak followed by the kurtosis. The last column is the difference between the average in both positions. Ideally, this difference would be naught because the method should be as immune to the movement of the sensor as possible. The closest averages are achieved by the cumulative kurtosis so overall, in this experiment, this method would be best option.

4.2. One gel pad with metallic interphase

This experiment uses only one gel pad with an aluminium plate at its base to simulate a different interphase where the echo is reflected, see Figure 13 case *b*. The signals are quite different from the first case due to the multipath echoes that originates with the multiple interfaces (where the shear waves in the metal propagate a lot faster than in the pad), see Figure 14.

Table 2: Time of arrival measurements of the echo for the two gel pads configuration.

	Horizontal		Slanted		
	Avg.	Std.	Avg.	Std.	Diff. Avg.
Xcorr.	40.15	0.210	40.40	0.443	−0.255
Max.	40.21	0.195	40.39	0.225	0.1728
Energy	40.04	0.138	39.55	0.349	−0.4808
AIC	39.98	0.168	39.32	0.274	−0.6616
Kurtosis	40.02	0.161	40.14	0.260	0.1184

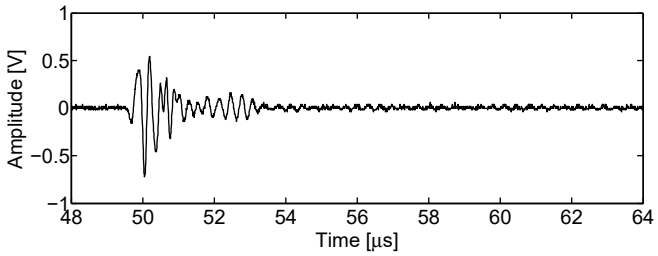

Figure 14: Echo in the gel-metal interphase when the sensor is slanted.

The results of the algorithms are given in Table 3 where the most accurate is the minimum cumulative energy (39.98 µs) followed by the kurtosis (39.95 µs) when the sensor is vertically aligned and the kurtosis (39.77 µs) when the sensor is slanted. In all cases, the kurtosis has the lowest standard deviation which also gives the most similar averages in both positions (0.1796 µs) and, again, turns to be the best option.

4.3. Human thigh

The results obtained in the calibration setups show that the algorithms are all of them reasonably accurate and precise in the measurements of the thickness of the gel pad, being the cumulative kurtosis the method with the best performance.

In the next experiment the objective was to measure the depth of the femur bone using a setup similar to the

Table 3: Time of arrival measurements of the echo for one gel pad with aluminium base configuration.

	Horizontal		Slanted		
	Avg.	Std.	Avg.	Std.	Diff. Avg.
Xcorr.	40.11	0.283	40.41	0.410	−0.300
Max.	39.75	0.148	40.40	0.360	−0.6540
Energy	39.98	0.103	39.64	0.253	0.3328
AIC	39.92	0.091	39.48	0.254	0.4367
Kurtosis	39.95	0.089	39.77	0.221	0.1796

one shown in Figure 3. The depth of the bone is, in this case, unknown, so the important parameter to evaluate is the deviation of the results. A large set of measurements was carried out with the sensor in the same position but with different angles with respect the thigh surface, measurements 1 to 10 in Table 4. Subsequently, all of them consist of 10 measurements shifting the position and angle of the sensor. The lowest standard deviations are highlighted with boxed values and the worst with bold fonts. The depth of the bone is determined with the average value corresponding to the method that gives the most stable results. Then, when the lowest standard deviation in the set of measurements number 3 corresponds to the cumulative kurtosis with a value of 0.224, the echo would be at 53.27 µs and the depth of the bone would be 4.00 cm. The overall results show that the lowest standard deviation is given by the cumulative kurtosis in six cases out of ten and the second to lowest in three more cases. The cumulative energy with negative slope has also good performance in three out of ten occasions. The algorithms based on the cross correlation and maximum peak algorithms show the worst behaviour. Then, considering that the kurtosis also had an outstanding accuracy in the tests with the gels, the most reliable measurements of the bone-depth would be given by this method.

Notice that the deviation of the measurements is always well below 500 microns giving an idea on the stability of the depth value even when the sensor was placed at different angles.

5. Conclusions

Commonly used 3D trackers offer the possibility of reliably record the movements and the positions of the human body using infrared reflective markers. The collected data is of great interest in a large number of application in health — like prosthetics design, gait analysis, rehabilitation therapy and so on. Crucially, by design, these systems are able to track points of the body located on the skin surface, while in several case the ability to measure the position of the bones would be of greater interest. A solution has been proposed that combine the surface markers with a ultrasound transceiver that can add to the marker position data the depth of the first bone surface underneath, enabling (when using a sufficient number of sensors) to estimate the absolute position of the bone.

In order to achieve a reasonable accuracy, it is quite important to be able to compute the depth of the main ultrasonic echo with the highest possible reliability. In this paper it is shown that the algorithm used to determine the time-of-flight of the echo is significant to this purpose; several commonly used algorithm — cross correlation, maximum peak, minimum energy, Akaike information criterion, and time series cumulative kurtosis — have been compared in three different experiments, modeling the scenario of a real-time, in vivo measurement.

The analysis of the resulting data sets points out that the overall best method is the cumulative kurtosis with the inclusion of a negative slope proposed in this paper, showing, on average, better repeatability (in the measurement where the depth of the interface where not known) and better accuracy (in the experiments where the nominal depth is known).

Acknowledgements

The authors would like to thanks the Center for Biomechanics and Rehabilitation Research, at Colorado School of Mines (Golden, CO, USA) for lending the sensors used in this measurement.

6. References

[1] Laurence Chéze. Comparison of different calculations of three-dimensional joint kinematics from video-based system data. *Journal of Biomechanics*, 33(12):1695–1699, dec 2000. doi: 10.1016/s0021-9290(00)00146-9. URL `http://dx.doi.org/10.1016/S0021-9290(00)00146-9`.

[2] Christine M Myles, Philip J Rowe, Colin R.C Walker, and Richard W Nutton. Knee joint functional range of movement prior to and following total knee arthroplasty measured using flexible electrogoniometry. *Gait & Posture*, 16(1):46–54, aug 2002. doi: 10.1016/s0966-6362(01)00198-9. URL `http://dx.doi.org/10.1016/S0966-6362(01)00198-9`.

[3] C. Reinschmidt, A.J. van den Bogert, B.M. Nigg, A. Lundberg, and N. Murphy. Effect of skin movement on the analysis of skeletal knee joint motion during running. *Journal of Biomechanics*, 30(7):729–732, jul 1997. doi: 10.1016/s0021-9290(97)00001-8. URL `http://dx.doi.org/10.1016/S0021-9290(97)00001-8`.

[4] Romano Giannetti, Anthony Petrella, Joel Bach, and Anne Silverman. Feasibility study of in vivo bone depth measurement using high frequency ultrasound. In *2015 IEEE International Instrumentation and Measurement Technology Conference (I2MTC 2015)*, pages 762–766, Pisa, Italy, May 2015.

[5] Fernando L. Arbona MD, Babak Khabiri DO, and John A. Norton DO. *Ultrasound-Guided Regional Anesthesia: A Practical Approach to Peripheral Nerve Blocks and Perineural Catheters (Cambridge Medicine)*, chapter 2. Cambridge University Press, 2011. ISBN 978-0521515785.

[6] Pascal Laugier and Guillaume Haïat. *Bone Quantitative Ultrasound*, page 39. Springer, 2010. ISBN 978-9400700164.

[7] P. Moilanen. Ultrasonic guided waves in bone. *Ultrasonics, Ferroelectrics, and Frequency Control, IEEE Transactions on*, 55(6):1277–1286, June 2008. ISSN 0885-3010. doi: 10.1109/TUFFC.2008.790.

[8] F William Mauldin, Kevin Owen Jr, Mohamed Tiouririne, and John A Hossack. The effects of transducer geometry on artifacts common to diagnostic bone imaging with conventional medical ultrasound. *Ultrasonics, Ferroelectrics, and Frequency Control, IEEE Transactions on*, 59(6):1101–1114, 2012.

[9] Tian-Shin Yeh, Chueh-Hung Wu, Wen-Shiang Chen, and Tyng-Guey Wang. Serial ultrasonography for early detection and follow-up of heterotopic ossification in stroke. *Journal of Medical Ultrasound*, 20(2):119–124, 2012.

[10] Rui Zheng, Lawrence H Le, Doug Hill, and Edmond Lou. Estimation of bone quality on scoliotic subjects using ultrasound reflection imaging method-a preliminary study. In *Ultrasonics Symposium (IUS), 2015 IEEE International*, pages 1–4. IEEE, 2015.

[11] Thomas Fuerst, Claus C. Glüer, and Harry K. Genant. Quantitative ultrasound. *European Journal of Radiology*, 20(3):188 – 192, 1995. ISSN 0720-048X. doi: http://dx.doi.org/10.1016/

Table 4: Time of arrival measurements of the echo in a human thigh. The best standard deviation results are marked inside a box whereas the worst are highlighted in bold font. The conclusions for the standard deviation are extrapolated to the average values.

	Average						Standard deviation					
	Xcorr	**Max**	**E(n)**	**AIC**	**K(n)**	**[cm]**	**Xcorr**	**Max**	**E(n)**	**AIC**	**K(n)**	**[cm]**
Set 1	49.54	49.83	51.20	**50.03**	51.36	3.84	1.165	1.823	0.606	**2.627**	0.740	0.045
Set 2	51.43	**49.68**	52.92	52.77	53.12	3.97	1.455	**1.677**	0.413	0.454	0.425	0.031
Set 3	49.27	**49.47**	53.15	52.94	53.27	4.00	0.489	**1.283**	0.334	0.392	0.224	0.017
Set 4	50.89	51.54	52.75	**51.35**	53.00	3.97	1.559	1.368	0.331	**3.940**	0.256	0.019
Set 5	51.82	**51.31**	53.27	53.02	53.45	3.98	1.373	**1.540**	0.448	0.294	0.434	0.022
Set 6	50.27	**50.29**	52.54	52.52	52.55	3.94	1.150	**1.413**	0.267	0.286	0.265	0.02
Set 7	50.67	**50.67**	52.23	52.07	52.37	3.93	0.833	**0.899**	0.494	0.505	0.367	0.028
Set 8	**52.25**	52.35	52.99	52.96	53.02	3.98	**0.880**	0.754	0.356	0.415	0.351	0.026
Set 9	**51.17**	50.77	51.83	51.76	52.08	3.91	**1.376**	0.532	0.415	0.416	0.338	0.025
Set 10	**50.48**	51.64	52.27	52.12	52.42	3.92	**1.772**	0.736	0.240	0.307	0.289	0.018

0720-048X(95)00650-F. URL http://www.sciencedirect.com/science/article/pii/0720048X9500650F.

[12] Robert S. Siffert and Jonathan J. Kaufman. Ultrasonic bone assessment: "the time has come". *Bone*, 40(1):5 – 8, 2007. ISSN 8756-3282. doi: http://dx.doi.org/10.1016/j.bone.2006.07.018. URL http://www.sciencedirect.com/science/article/pii/S8756328206006247.

[13] K. Rohde, D. Rohrbach, C.C. Glüer, P. Laugier, Q. Grimal, K. Raum, and R. Barkmann. Influence of porosity, pore size, and cortical thickness on the propagation of ultrasonic waves guided through the femoral neck cortex: a simulation study. *Ultrasonics, Ferroelectrics, and Frequency Control, IEEE Transactions on*, 61(2):302–313, February 2014. ISSN 0885-3010. doi: 10.1109/TUFFC.2014.6722615.

[14] Haijiang Zhang, Clifford Thurber, and Charlotte Rowe. Automatic p-wave arrival detection and picking with multiscale wavelet analysis for single-component recordings. *Bulletin of the Seismological Society of America*, 93(5):1904–1912, 2003. doi: 10.1785/0120020241. URL http://www.bssaonline.org/content/93/5/1904.abstract.

[15] Jochen H. Kurz, Christian U. Grosse, and Hans-Wolf Reinhardt. Strategies for reliable automatic onset time picking of acoustic emissions and of ultrasound signals in concrete. *Ultrasonics*, 43 (7):538 – 546, 2005. ISSN 0041-624X. doi: http://dx.doi.org/10.1016/j.ultras.2004.12.005. URL http://www.sciencedirect.com/science/article/pii/S0041624X04003166.

[16] C.D. Saragiotis, L.J. Hadjileontiadis, and S.M. Panas. Pai-s/k: A robust automatic seismic p phase arrival identification scheme. *Geoscience and Remote Sensing, IEEE Transactions on*, 40(6):1395–1404, Jun 2002. ISSN 0196-2892. doi: 10.1109/TGRS.2002.800438.

[17] Guillermo Robles, José Manuel Fresno, and Juan Manuel Martínez-Tarifa. Separation of radio-frequency sources and localization of partial discharges in noisy environments. *Sensors*, 15(5):9882–9898, Apr 2015. ISSN 1424-8220. doi: 10.3390/s150509882. URL http://dx.doi.org/10.3390/s150509882.

[18] P. Wagenaars, P.A.A.F. Wouters, P. van der Wielen, and E.F. Steennis. Accurate estimation of the time-of-arrival of partial discharge pulses in cable systems in service. *Dielectrics and Electrical Insulation, IEEE Transactions on*, 15(4):1190–1199, August 2008. ISSN 1070-9878. doi: 10.1109/TDEI.2008.4591242.

[19] Young-Chul Choi, Jin-Ho Park, and Kyoung-Sik Choi. An impact source localization technique for a nuclear power plant by using sensors of different types. {*ISA*} *Transactions*, 50(1): 111 – 118, 2011. ISSN 0019-0578. doi: http://dx.doi.org/10.1016/j.isatra.2010.08.004. URL http://www.sciencedirect.com/science/article/pii/S0019057810000728.

[20] P.J. Moore, IE. Portugués, and IA Glover. Radiometric location of partial discharge sources on energized high-voltage plant. *Power Delivery, IEEE Transactions on*, 20(3):2264–2272, July 2005. ISSN 0885-8977. doi: 10.1109/TPWRD.2004.843397.

[21] Young-Chul Choi, Jin-Ho Park, and Kyoung-Sik Choi. An impact source localization technique for a nuclear power plant by using sensors of different types. *ISA transactions*, 50(1):111–118, 2011.

[22] Sinan Gezici. A survey on wireless position estimation. *Wireless personal communications*, 44(3):263–282, 2008.

[23] Xiaoming Lai and H. Torp. Interpolation methods for time-delay estimation using cross-correlation method for blood velocity measurement. *IEEE Transactions on Ultrasonics, Ferroelectrics, and Frequency Control*, 46(2):277–290, March 1999. ISSN 0885-3010. doi: 10.1109/58.753016.

[24] C. Knapp and G. Clifford Carter. The generalized correlation method for estimation of time delay. *Acoustics, Speech and Signal Processing, IEEE Transactions on*, 24(4):320–327, Aug 1976. ISSN 0096-3518. doi: 10.1109/TASSP.1976.1162830.